ISPRS Journal of Photogrammetry and Remote Sensing 120 (2016) 84–98

Contents lists available at ScienceDirect

ISPRS Journal of Photogrammetry and Remote Sensing

journal homepage: www.elsevier.com/locate/isprsjprs

Disaster debris estimation using high-resolution polarimetric stereo-SAR

Christian N. Koyama [a,*], Hideomi Gokon [b], Masaru Jimbo [c], Shunichi Koshimura [c], Motoyuki Sato [a]

[a] Tohoku University, Center for Northeast Asian Studies (CNEAS), 41 Kawauchi, 980-8576 Sendai, Japan

[b] The University of Tokyo, International Center for Urban Safety Engineering (ICUS), Institute of Industrial Science, 4-6-1 Komaba, 153-8505 Tokyo, Japan

[c] Tohoku University, International Research Institute of Disaster Science (IRIDeS), 468-1 Aoba, 980-0845 Sendai, Japan

A R T I C L E I N F O

Article history:
Received 18 January 2016
Received in revised form 26 July 2016
Accepted 8 August 2016
Available online 16 September 2016

Keywords:
Debris
Disaster mitigation
Radargrammetry
Radar polarimetry
Synthetic aperture radar (SAR)
Tsunami

A B S T R A C T

This paper addresses the problem of debris estimation which is one of the most important initial challenges in the wake of a disaster like the Great East Japan Earthquake and Tsunami. Reasonable estimates of the debris have to be made available to decision makers as quickly as possible. Current approaches to obtain this information are far from being optimal as they usually rely on manual interpretation of optical imagery. We have developed a novel approach for the estimation of tsunami debris pile heights and volumes for improved emergency response. The method is based on a stereo-synthetic aperture radar (stereo-SAR) approach for very high-resolution polarimetric SAR. An advanced gradient-based optical-flow estimation technique is applied for optimal image coregistration of the low-coherence non-interferometric data resulting from the illumination from opposite directions and in different polarizations. By applying model based decomposition of the coherency matrix, only the odd bounce scattering contributions are used to optimize echo time computation. The method exclusively considers the relative height differences from the top of the piles to their base to achieve a very fine resolution in height estimation. To define the base, a reference point on non-debris-covered ground surface is located adjacent to the debris pile targets by exploiting the polarimetric scattering information. The proposed technique is validated using in situ data of real tsunami debris taken on a temporary debris management site in the tsunami affected area near Sendai city, Japan. The estimated height error is smaller than 0.6 m RMSE. The good quality of derived pile heights allows for a voxel-based estimation of debris volumes with a RMSE of 1099 m^3. Advantages of the proposed method are fast computation time, and robust height and volume estimation of debris piles without the need for pre-event data or auxiliary information like DEM, topographic maps or GCPs.

1. Introduction

Geophysical disasters like earthquakes, tsunamis, floods, landslides, etc., result in disaster debris. The removal and management of debris generated in such events is a major challenge in the immediate aftermath as well as the longer-term recovery efforts. The debris generated by tsunamis is often more complicated to handle and causes more problems than other types of disaster debris. This is due to a number of factors: (i) Unlike an earthquake, a tsunami usually moves a substantial amount of debris from its origin location and deposits it chaotically across the inundated area. (ii) The tsunami wave thereby mixes up materials from everything in its path, causing various kinds of debris to be combined into piles. (iii) Vast quantities of debris are usually carried back into the sea by the returning waves with the heavy materials being deposited in the coastal area and the lighter ones floating out to the sea where they can remain for month or years causing a number of hazards to marine environment, shipping and fishing industry. (iv) The tsunami waves can also transport large volumes of marine sediments inland. Depending on the quality of sediments and where they have been deposited, they usually have to be handled as disaster debris as well. As this study will deal with the estimation of debris volumes deposited on the affected land surface, special attention has to be paid to factors (i), (ii) and (iv).

The challenges caused by tsunami debris are urgent. Apart from the inspection for victims, the most urgent task is the removal of debris from roads in order to allow rescue workers gain access to the affected areas. This makes the localization and estimation of debris volumes one of the most important initial challenges in the wake of a disaster. In order to scope the damage and coordinate

* Corresponding author.
E-mail addresses: christian.koyama@cneas.tohoku.ac.jp, christian.koyama@outlook.com (C.N. Koyama).

http://dx.doi.org/10.1016/j.isprsjprs.2016.08.003
0924-2716/

the response, it is prerequisite that reasonable estimates of the disaster debris in terms of amount and distribution are available to decision makers as quick as possible. Being logistically challenging, time consuming and potentially dangerous, debris estimates are rarely computed from ground based information but usually rely on satellite or aerial photographs (Hansen et al., 2007). However, optical sensors either space- or airborne cannot operate during night or clouded conditions. Furthermore, the interpretation of a debris strewn landscape from 2D photographs alone cannot provide detailed information about the volume of deposited piles and thus the computation requires considerable experience and expert knowledge to yield somewhat reliable estimates. A faster and more powerful method for debris volume estimation could considerably improve the disaster mitigation in the direct aftermath of such a large scale disaster. As the overall debris management is a multi-billion dollar operation, more accurate estimations of the debris volume would also help to significantly reduce the economic impacts.

This motivates us to develop a method for improved debris volume estimation from multi-angular fully polarimetric Synthetic Aperture Radar (PolSAR) data in this paper. Due to the active illumination and cloud penetration of a SAR, the proposed approach has the advantage to provide debris estimates at night or other atmospheric conditions under which optical sensors cannot operate. Moreover the use of polarimetric SAR stereographic height estimation allows obtaining detailed information about the 3D structure of the debris providing much richer *a priori* information to decision makers planning the initial rescue and clean up measures as well as the following long-term waste management operations. We use the March 11 2011 Great East Japan Tsunami as case study for the development and validation of the novel approach.

The severity of the tsunami attack on the Pacific coast of Northeastern Japan was unprecedented in both height and reach. In principle Japan's entire east coast was impacted by the tsunami. However, the by far most heavily affected areas were in the three prefectures closest to the epicenter, Miyagi, Fukushima and Iwate (Fig. 1). Despite Japan being considered as one of the best disaster-prepared countries in the world, the tsunami caused the loss of nearly 20,000 people and damaged hundreds of thousand houses and other buildings. The National Police Agency has confirmed 15,891 deaths and 2584 people missing and a total of 129,225 buildings and/or houses completely destroyed or washed away. Due to the vastness of destruction, the tsunami created extensive volumes of debris making the debris management operation the largest and most expensive of its kind in the world (Ranghieri and Ishiwatari, 2014). Anything standing in the way was instantly turned into disaster debris and swept away often by several hundred meters or more (Tanikawa et al., 2014). Large amounts of sediments, up to 20% of the total estimated debris in some areas, were deposited on the land (Goto et al., 2014). In the most extreme case of Ishinomaki city, the tsunami generated an estimated 6.16 Mt of debris – equivalent to more than 100 years of waste production under normal circumstances (UNEP, 2012). Fig. 1 provides a map of debris volumes for the most affected cities in Tohoku as estimated by the Sendai municipal government (Sendai City Environmental Bureau, 2012). The Tohoku (literally "East North") region consists of the six prefectures in the north of Japan's largest island, Honshu.

Based on post-event airborne SAR imaging campaigns in the area, we develop a method for robust and fast estimation of heights and volumes of debris piles. State-of-the-art high-resolution fully polarimetric X-band SAR data of the Japanese *P*olarimetric *i*nterferometric *S*ynthetic *A*perture *R*adar 2 (Pi-SAR2) operated by the National Institute of Communication and Information Technology (NICT) (Satake et al., 2013; Yamaguchi et al., 2014) is used which

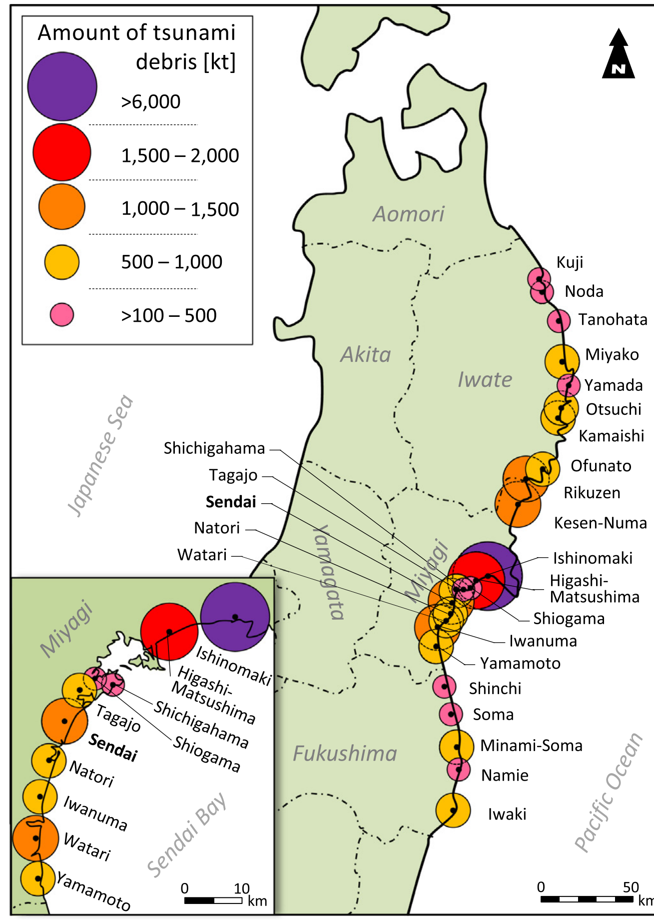

Fig. 1. Map of the Tohoku region in Northeastern Japan showing the amounts of tsunami debris in the most affected cities along the Pacific coast.

were acquired in square-flight path campaigns (Fig. 2) over the Sendai area (Koyama et al., 2014; Koyama and Sato, 2014).

Numerous studies dealing with investigation and mitigation of the earthquake and tsunami impacts using SAR and PolSAR data have been published since the event. Chen and Sato (2013), Satake et al. (2012) and Watanabe et al. (2012) demonstrated detection and analysis of coarse scale damaged areas based on polarimetric target decomposition techniques. Yulianto et al. (2015) proposed semiautomic unsupervised change-detection to map flooded areas using multi-temporal single polarization ALOS/PALSAR data. However, as these approaches are all based on change detection techniques using pre- and post-event SAR data they cannot be applied in cases in which (suitable) pre-event data is not available. Kobayashi et al. (2012a) and Sato et al. (2012) studied the Pi-SAR2 data taken immediately in the aftermath of the event, on March 12 and 18, 2011, demonstrating the potential to detect flooded areas and damaged urban areas by fully polarimetric data without the need for pre-event data. Sato et al. (2007) presented a hybrid scheme based on scattered power decomposition and scattering feature extraction to classify buildings damaged after an earthquake. Aoki et al. (2013) and Arii et al. (2014) developed a novel approach to track floating debris on the sea surface based on ship detection methods which allows obtaining information about the amounts of debris as well as about their vector velocities. Even though no pre-event data is used, the method is not a tool for immediate disaster response as it requires a multitude of SAR imagery and relies on time series analysis. Principally, a method that only requires limited post-event SAR

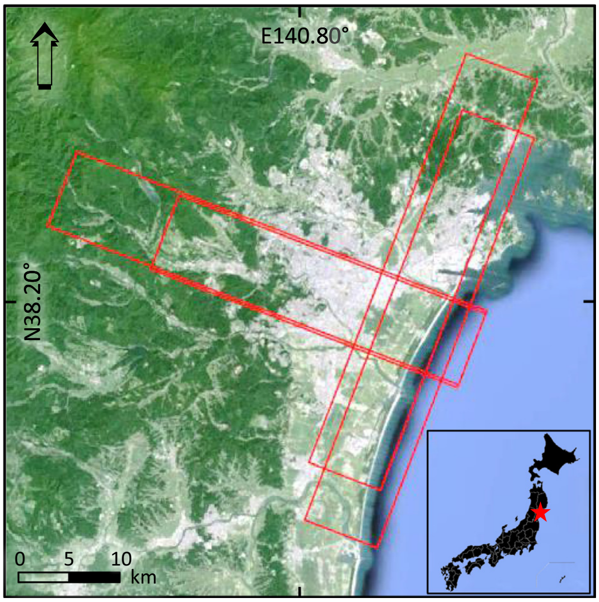

Fig. 2. Pi-SAR2 square-flight paths over the Sendai area.

data is highly desirable to increase the general applicability. Moreover the method should be suitable to deliver results as quickly as possible after a disaster. We will discuss the development of just such a method in this paper. In the following section we introduce the ground based debris observations and the SAR data used in this study. In Section 3, the methodology of the debris estimation, including the steps of image coregistration, polarimetric scattering decomposition and stereo-SAR height retrieval, is elucidated. The results are discussed in Section 4 before Section 5 concludes the paper.

2. Materials

2.1. Pi-SAR2 data

NICT started development of the high performance airborne Pi-SAR2 since 2006, as a successor to the Pi-SAR (X-band). The initial demonstration flight was conducted in December 2008 and the system is fully operational since 2010. The Pi-SAR2 instruments are installed to a Grumman Gulfstream II business jet. To realize simultaneous polarimetric and interferometric observations, three slotted waveguide planar array antennas (two vertical polarized antennas and one horizontal polarized antenna) are installed in two radomes at the left and right sides of an airplane. The perpendicular baseline between the main antenna (left) and the auxiliary antenna (right) is 2.6 m.

Pi-SAR2 has polarimetric and interferometric functions with high spatial resolution of 0.3–0.6 m in along-track (azimuth) direction and 0.3–0.5 m in cross-track (slant-range) direction at X-band with a center frequency of 9.65 GHz. The ground height (DEM) accuracy for the cross-track interferometric imagery is in the order of 2 m (Kobayashi et al., 2012b, 2014). High resolution in range direction is achieved by wide transmission bandwidth of 500 MHz. Noise equivalent backscattering coefficient (NEσ0) is kept under -27 dB in slant-range distance of 5–10 km between incidence angles from 20° to 60° at the platform altitude of 12,000 m (Matsuoka et al., 2009; Satake et al., 2011, 2013). The square-flight data used in this study was acquired at altitudes of approx. 8800 m.

Table 1 gives an overview of the Pi-SAR2 images used in this study. Square-flight imaging campaigns were conducted on four different dates, namely August 26 and October 17, 2013, June 22, 2014 and March 5, 2015. The four imaging swaths for the E-W, W-E, N-S and S-N tracks are shown in Fig. 2. The across track separation for two parallel flights ranges between 15,957 and 17,105 m. Fig. 3 shows a set of four square flight images of the target area as acquired on August 26, 2013. Note that due to a sensor malfunction, for the last campaign only one pair of parallel flights, in E-W and W-E direction, was acquired. The average temporal baseline is less than 10 min for a pair of two parallel flight pass in opposite directions. The maximum baseline between the first and last (orthogonal) pass is in the order of 40 min.

2.2. Study area and in situ debris observations

The study area is situated at the Sendai coast 10 km east of the downtown and 87 km west of the epicenter of the Great East Japan Earthquake. The first tsunami wave struck the area at 15:30, 45 min after the main shock. With 246,628 buildings and houses damaged or destroyed, estimates from Sendai municipal authorities indicate the disaster generated 1.35 Mt of debris and some 1.3 Mt of tsunami sediment in the area alone (Sendai City Environmental Bureau, 2012). After one year almost all loose debris from the impacted area has been collected and moved to interim and final storage locations. Within four months after the disaster, three new temporary incinerators, with a combined

Table 1
Overview of the Pi-SAR2 square-flight data taken over the study area.

No.	Date	Path, direction	Start (JST)	LIA [°][a]	Altitude [m]
1	2013/8/26	Flight-3, EW	10:37	51.56	8760
2	2013/8/26	Flight-4, WE	10:47	35.01	8756
3	2013/8/26	Flight-8, NS	11:39	46.69	8758
4	2013/8/26	Flight-9, SN	11:48	42.60	8753
5	2013/10/17	Flight-15, EW	14:08	47.12	8785
6	2013/10/17	Flight-16, WE	14:18	37.31	8786
7	2013/10/17	Flight-18, NS	14:37	48.28	8786
8	2013/10/17	Flight-19, SN	14:48	39.15	8782
9	2014/6/22	Flight-2, NS	12:18	48.57	9235
10	2014/6/22	Flight-3, SN	12:27	36.17	9234
11	2014/6/22	Flight-4, EW	12:46	49.54	9236
12	2014/6/22	Flight-5, WE	12:56	34.87	9232
13	2015/3/5	Flight-5, EW	10:27	49.53	9240
14	2015/3/5	Flight-6, WE	10:36	38.38	9242

[a] Mean local incidence angle at the Ido debris storage site.

processing capacity of 480 t/day, were commissioned at the three principal debris management sites in the area, namely Gamo, Arahama and Ido. The destruction of coastal forests and wooden houses by the tsunami created a large number of piles of timber. As the wooden debris has the lowest priority in the waste management (Asari et al., 2013), it was only partially moved to the storage sites while a large number of smaller piles remained distributed over the area at their original locations. Due to this fact we could still find a number of smaller quasi unaltered tsunami debris piles consisting mainly of wooden components mixed with soil in the area in late 2013. These piles are considered to represent best the real situation of the immediate disaster aftermath (Suppasri et al., 2012).

In situ debris measurements, which are used as reference data for the following analysis, were carried out at both the Arahama and Ido temporary debris management sites (Fig. 3) one day prior to the Pi-SAR2 acquisitions. Fig. 4 shows optical images taken at the Ido site on Aug. 25, 2013 and Fig. 5 shows a Yamaguchi 4-component (Y4C) decomposition color composite image (Yamaguchi et al., 2006) of the site taken on Aug. 26, 2013. The detailed structures within the compartments are well visible. Bare soil surface shows in blue, while the green areas indicate the presence of some vegetation cover which is composed mostly of some salt resistant grass and bush species. Strong double bounce scattering in red can be seen from metal structures oriented perpendicular to the look direction along the canal. The very bright features in the N-E corner of the storage site corresponds to a temporary incinerator with a metal smoke stack of approx. 15 m height and a waste conveyer (Fig. 4). The debris piles were composed of different materials, e.g. metal, wood or rubble, and stored at the Ido yard

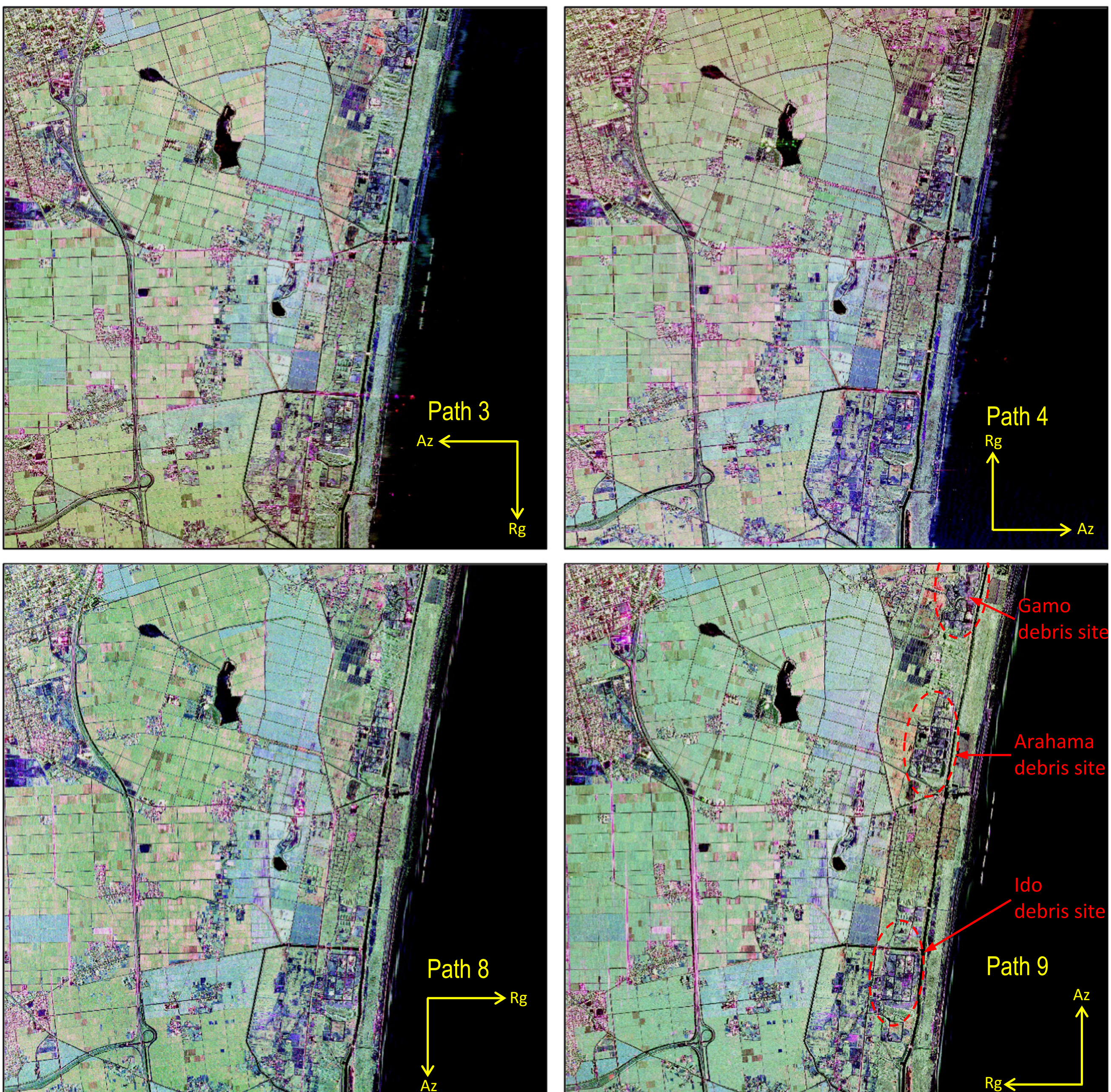

Fig. 3. Orthorectified full polarimetric Pi-SAR2 square-flight path ground-range Pauli RGB images (|HH − VV|, |HV + VH|, |HH + VV|) of the tsunami affected coastal area near Sendai. The images were acquired on August 26, 2013 and have a size of 24,000 × 24,000 pixels. © NICT 2013.

for further processing. Waste was segregated into various piles consistent with the national guidelines. The size (height, base area), shape and location of tsunami debris piles were measured on the ground by using total station, laser range finder and GPS at the storage site. Fig. 6 shows the scheme of ground based debris measurements. For (quasi) rectangular shapes, GPS coordinates were recorded at the four corners (Fig. 6a) and used to compute the GIS polygons with width and length (Fig. 6b). For round shaped piles only the GPS coordinates of the most northern point was recorded, height and width were measured according to Fig. 6c. In the case of complex shapes (Fig. 6d), the piles were divided into basic shapes by measuring all the required multiple heights and widths. Examples of debris piles of different materials and shapes are shown in Fig. 7. Following the guidelines for estimating the total gross volume of piled logging debris as proposed by Hardy (1996), sampled piles were categorized into seven generalized pile shapes (Fig. 8), or combinations of these. Subsequently, the volumes were calculated using appropriate volumetric formulae with the in situ measured height, length and width dimensions. Table 2 exemplarily summarizes the ground based debris information for 21 individual piles as assessed at the Ido site one day prior the August 26 2013 Pi-SAR2 campaign. Note that due to the ongoing processing of the waste, the sizes and shapes of the piles varied between the different acquisition dates. Altogether 53 piles were considered in the analysis.

3. Methods

This section discusses in detail the exact methodology of the proposed polarimetric stereo SAR based debris height and volume estimation. Fig. 9 shows the workflow of the developed method. It is important to note that prior to the image coregistration, addressed in the following section, all Pi-SAR2 images are projected onto a common ground range plane. In Section 3.2, we elucidate the polarimetric processing including the target decomposition and describe the subsequent reference point and shape outline extraction. Two different polarimetric speckle filters are applied to optimize both the shape outline extraction and the height retrieval. Moreover, both model based decomposition and eigenvalue based decomposition are performed to allow robust echo time calculations by using only odd bounce scattering contributions and to achieve a more stable retrieval of the reference ground heights, respectively. Finally, the original radargrammetric approach for the pixel-wise debris height and voxel-based volume estimation is presented in Section 3.3.

3.1. Image coregistration

The coregistration is the first processing step to convert the images into a common spatial grid. The quality of this image coregistration is one of the critical factors in applications like change detection, InSAR and stereo SAR. Conventional methods for coregistration are based on the (complex) cross-correlation of the images. The process usually consists of two main steps. First, cross correlation is applied to determine the best integer translation vector for the coarse alignment of the images. In the second step images are upsampled before repeating the same procedure to determine the subpixel relative offset. Despite its simple implementation, the use of interpolation prior to cross-correlation suffers from a high computational load. Moreover, for very high resolution data over complicated terrain with largely varying azimuthal illumination angles, the results, especially when using only intensity information when the data does not satisfy interferometric conditions, are usually not good enough for the given task of this study. As the square-flight images are in non-interferometric conditions, a variable bias of coregistration exists all over the scene

Fig. 4. Optical photographs showing (a) a panoramic view taken at the south end of the storage site looking north and (b) a close up image taken at the Ido temporary debris management site on August 25, 2013.

due to the different illumination angles and polarizations. In addition, methods exploiting the interferometric phase differences between the images are not applicable. Another challenge is introduced due to the fact that for fully polarimetric SAR data, the image characteristics can be very different depending on the polarization. Chureesampant and Susaki (2011) proposed a coregistration method based on ground control points (GCP) driven SIFT (*S*cale *I*nvariant *F*eature *T*ransformation) algorithm using only the total power. However, this approach only works on the coarse scale and is not useful for the sub-meter resolution we are interested in. For a more robust coregistration of high-resolution multi-angular non-interferometric SAR data, Dell'Acqua et al. (2004) developed a method based on crossroad and road junction extraction and matching. However, while this approach has advantages when using images acquired in different polarizations and from different directions, it also requires considerable processing effort, auxiliary data, and might not be reliable in a disaster situation when roads are destroyed, flooded or covered with debris.

To overcome these issues, we choose to apply a nonrigid stereo coregistration technique capable of locally warping the slave images to align with the master image using the eFolki (*e*xtended *F*lot *O*ptique par *L*ucas–*K*anade *I*térratif) method (Plyer et al., 2014). The eFolki algorithm is a fast and robust optical-flow estimation technique derived from the Lucas-Kanade (LK) gradient-based approach for stereo vision (Le Besnerais and Champagnat, 2005; Lucas and Kanade, 1981). Adaption of the algorithms for SAR coregistration has been demonstrated recently by Plyer et al. (2015).

After performing ground range projection to bring all images to a common ground plane $S \in R^2$, we consider the coregistration of two images I_1 and I_2 as defined on the 2-D support S. The displacement between both images, referred to as dense optical flow in optics, is defined by u: $x \to u(x) \in R^2$. The LK algorithm is a local window-based approach where $u(x)$ is defined as the minimizer of a criterion $J(u;x)$ computed over a local window with its center pixel x with

$$J(u;x) = \sum_{x' \in S} w(x'-x)(I_1(x') - I_2(x'+u(x)))^2 \tag{1}$$

where w is a separable Gaussian weighting function of limited support, which is typically a square $(2r+1) \times (2r+1)$ window defined by its in radius r.

The minimization procedure is carried out by an iterative Gauss-Newton strategy based on a first-order Taylor expansion of the intensity around a previous guess of the displacement u_k. Note that this makes LK a gradient-based approach, as opposed to block matching by exhaustive search over a limited area. In addition, modern LK algorithms use a pyramid of images to compute u at varying scale and are thereby not only iterative but also multiresolution.

In the eFolki, Eq. (1) is modified to

$$J(u;x) = \sum_{x' \in S} w(x'-x)(R(I_1)(x') - R(I_2)(x'+u(x)))^2 \tag{2}$$

where $R(I_i)$ is a rank function applied to the image I_i based on the local intensity-level ordering to compute the filtered value. It is given by

$$R(I)(x) = \#\{x' : \; x' \in S_R(x) \text{ with } |I(x)| > |I(x')|\} \tag{3}$$

where $S_R(x)$ is a neighborhood of x.

This rank transform has the effect of a nonlinear filter compressing the signal dynamics. From the 2^{32} levels of the float signal

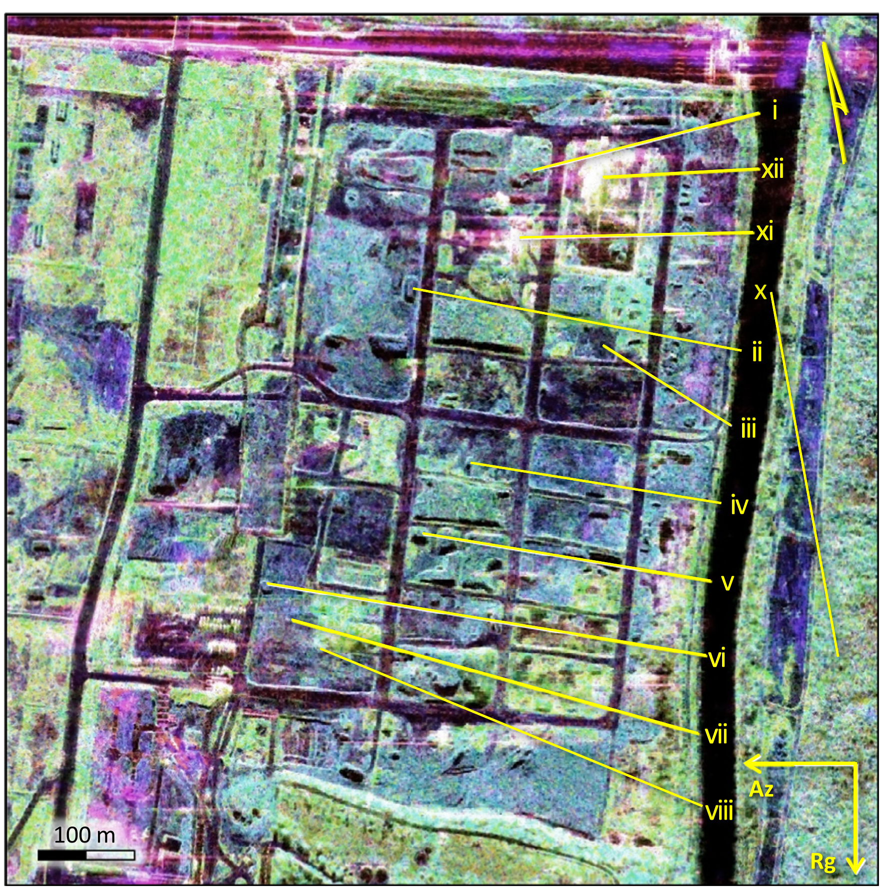

Fig. 5. Y4C RGB image of the Ido temporary tsunami debris management site.

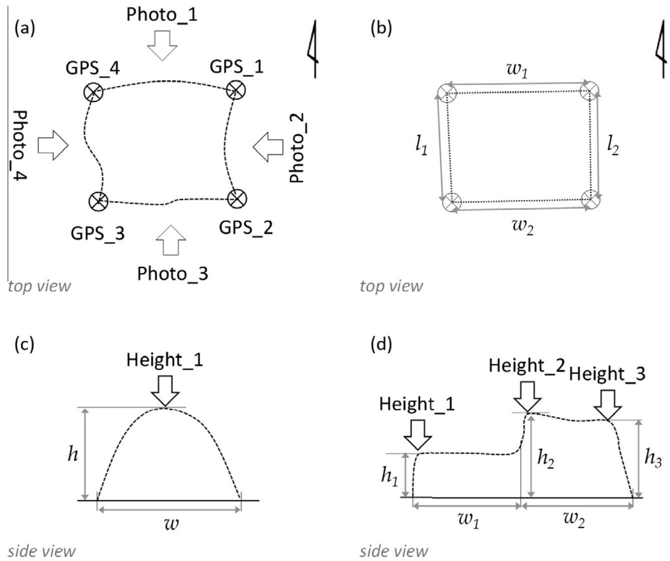

Fig. 6. Scheme of ground based piles size assessment with (a) arrangement of GPS coordinates and photographs, (b) resulting polygon shape, height and width measurement for (c) simple shape and (d) complex shapes.

forming the SAR image in each polarization, the rank gives a signal of $d^2 - 1$ levels where d is the rank filter window diameter. This compression effect on the signals' gradients drastically increase the robustness of the displacement estimation and enables the ability to compute the pixel motion between relatively different SAR images as caused by the azimuthal angle variations in the square-flight configuration. A comprehensive explanation of the full algorithm is provided in Plyer et al. (2014). It is important to point out that in this study the images were speckle filtered with two different techniques and the products were coregistered separately. For the main task of radargrammetric height estimation the Pi-SAR2 data was filtered using a 5 × 5 Gaussian filter to smooth out the very small scale heterogeneities of the debris piles (Fig. 10f). To best preserve the edges of the piles for the feature extraction a (refined) Lee filter with 5 × 5 kernel size was applied (Lee, 1981). Fig. 10a–d shows the result of coregistered Lee-filtered Pi-SAR2 square flight imaged debris field at the Ido yard.

The advantages of the applied methods include the following important aspects. The method manages to coregister non-interferometric data with low-coherence resulting from the illumination from opposite directions and in different polarizations over complicated terrain. Neither the relative phases nor auxiliary information such as orbits or DEM are required. The displacement is evaluated for each pixel and thus does not require the use of GCP. As the algorithm does not use polynomial regression, it can adapt well to the various kinds of deformation between the images even in the small-scale relief changes over debris piles. The procedure significantly reduces the computational costs compared to conventional coregistration methods (Plyer et al., 2014). Finally, the suitability to use pyramids of images offers opportunities to generate multiresolution stereo SAR data by combining two different sensors.

3.2. Polarimetric scattering decomposition

For PolSAR data, in the linear HV polarization basis, the observed fully polarimetric radar reflection can be represented in the form of the scattering matrix which we write as

$$S = \begin{bmatrix} S_{HH} & S_{HV} \\ S_{VH} & S_{VV} \end{bmatrix} \tag{4}$$

where S_{HV} denotes the complex backscattering coefficient for the horizontally polarized transmit and vertically polarized receive case.

Subject to reciprocity ($S_{HV} = S_{VH}$), in a monostatic system the Pauli scattering vector k_p is given by

$$k_p = \frac{1}{\sqrt{2}}[S_{HH} + S_{VV} \quad S_{HH} - S_{VV} \quad 2S_{HV}] \tag{5}$$

The 3 × 3 polarimetric coherency target matrix T_3 follows as

$$T_3 = \left\langle k_p k_p^H \right\rangle = \begin{bmatrix} T_{11} & T_{12} & T_{13} \\ T_{21} & T_{22} & T_{23} \\ T_{31} & T_{32} & T_{33} \end{bmatrix} \tag{6}$$

where $\langle \ldots \rangle$ indicates spatial ensemble averaging, k_p^H is the conjugate transpose of k_p and T_{ij} is the (i, j) element of T_3.

Note that since in this study we are mostly interested in the low entropy surface odd-bounce contributions to define the reference height, no orientation compensation by rotation of the T_3 matrix is required.

Model-based polarimetric decomposition is a powerful tool to understand the underlying scattering mechanisms. A general decomposition framework for an observed coherency T_3 matrix, is (Chen et al., 2014)

$$T_3 = f_v\langle T_{vol}\rangle + f_d T_{dbl} + f_o T_{odd} + f_h\langle T_{hel}\rangle + \cdots + T_{res} \tag{7}$$

where $\langle T_{vol}\rangle$, T_{dbl}, T_{odd} and $\langle T_{hel}\rangle$ indicate coherency matrices for the volume, double-bounce, odd-bounce and helix scattering components, respectively. f_v, f_d, f_o and f_h are the corresponding real-valued model coefficients. Satisfying a determined equation system, any possible scattering model can be included into (7). The residual matrix T_{res} is used to measure how well those models fit the observations. However, the nonlinear residual minimization optimization for (7) is computationally expensive and such a fine scattering mechanism interpretation is not needed in this study. For the timely emergency response, model-based decomposition of computation efficiency is preferred. In this study, the Yamaguchi four-component decomposition without orientation compensation (Yamaguchi et al., 2006) is adopted.

As we are not interested in the accurate separation between volume and double-bounce terms here, and for the sake of computational simplicity, a randomly oriented dipole model is employed for the volume scattering with

$$\langle T_{vol}\rangle = \frac{1}{4}\begin{bmatrix} 2 & 0 & 0 \\ 0 & 1 & 0 \\ 0 & 0 & 1 \end{bmatrix} \tag{8}$$

The double-bounce scattering model is based on the assumption of double reflections from right angle ground-wall structures. The resulting coherency matrix for double-bounce scattering is

$$T_{dbl} = f_d\begin{bmatrix} |\alpha|^2 & \alpha & 0 \\ \alpha^* & 1 & 0 \\ 0 & 0 & 0 \end{bmatrix} \tag{9}$$

where α is a parameter in terms of the reflection coefficients for EM waves with horizontal and vertical polarization from the ground and vertical surfaces.

The odd-bounce scattering model is used to represent the Bragg scattering phenomena from slightly rough surfaces where the cross-polarization component is negligible (Cloude and Pottier, 1996; Freeman and Durden, 1998). The corresponding coherency matrix formulation has the form

$$T_{odd} = f_o\begin{bmatrix} 1 & \beta^* & 0 \\ \beta & |\beta|^2 & 0 \\ 0 & 0 & 0 \end{bmatrix} \tag{10}$$

Fig. 7. Examples of different debris piles used in this study. Locations of piles i–viii at the Ido site are indicated in Fig. 5. Piles ix and x were located outside the management sites and represent quasi-unaltered conditions as found in the direct tsunami aftermath.

where β is a parameter in terms of the reflection coefficients for EM waves with horizontal and vertical polarization from the ground surfaces.

In order to account for the more general nonreflection symmetric scattering case encountered in complicated geometric structures, as e.g. can be expected in the case of disaster debris piles, the fourth model is equivalent to a helix scattering power (Krogager and Freeman, 1994). The two scattering matrices for left and right helix yield the corresponding coherency matrices given by

$$\langle T_{l-hel}\rangle = \frac{1}{2}\begin{bmatrix} 0 & 0 & 0 \\ 0 & 1 & -j \\ 0 & j & 1 \end{bmatrix} \quad \text{and} \quad \langle T_{r-hel}\rangle = \frac{1}{2}\begin{bmatrix} 0 & 0 & 0 \\ 0 & 1 & j \\ 0 & -j & 1 \end{bmatrix} \tag{11}$$

where j denotes the imaginary unit.

The scattering powers of each of the four main mechanism can be obtained with this model-based decomposition technique. They are represented by P_v, P_d, P_o and P_h for the volume, double-bounce, odd-bounce and helix scattering mechanisms, respectively. Subsequently, the dominant scattering mechanism can be determined for each Pi-SAR2 resolution cell. In Fig. 5 we can note green colors above the debris piles indicating strong received power in the T_{vol} channel. Note that this can result from both real volume scattering or misinterpreted double bounce terms resulting from random azimuthal orientation of debris pieces. It is important to point out that to avoid unwanted multiple scattering contributions which could hamper the accuracy of the subsequent echo time computation, we use only the odd-bounce components T_{odd} in the radargrammetric height estimation process.

In order to make more robust the identification of the pile base reference height estimation, to be discussed in the following section, we additionally make use of an eigenvalue decomposition of the T_3 coherency matrix as shown in (12) (Cloude and Pottier, 1996).

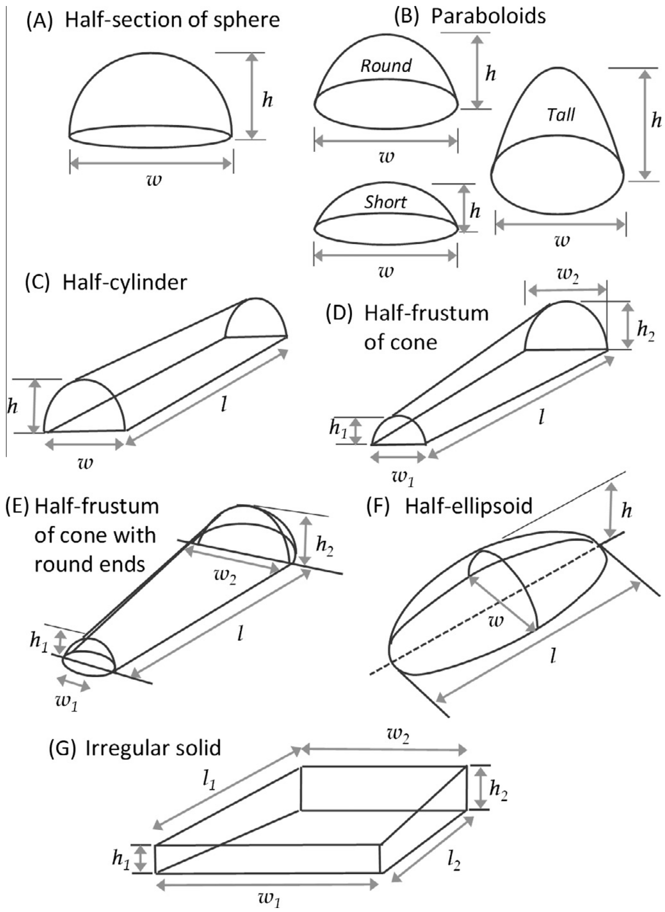

Fig. 8. Seven generalized pile shapes are used to represent the possible configurations of piled disaster debris.

$$\langle T_3 \rangle = [\underline{e}_1 \quad \underline{e}_2 \quad \underline{e}_3] \begin{bmatrix} \lambda_1 & 0 & 0 \\ 0 & \lambda_2 & 0 \\ 0 & 0 & \lambda_3 \end{bmatrix} [\underline{e}_1 \quad \underline{e}_2 \quad \underline{e}_3]^{*T} \tag{12}$$

where $\underline{e}_i$ are the eigenvectors and λ_i are the eigenvalues of the coherency matrix, respectively.

The spread of total scattered power across the eigenvalues is a good indicator of depolarization. As demonstrated by Cloude and Pottier (1997) and Lee et al. (1999) this can be used for quantitative measure by normalizing the eigenvalues to unit sum which can be interpreted as probabilities Pr_i of the statistically independent polarized states defined by the eigenvectors $\underline{e}_i$. The spread of probabilities can then be represented by the entropy H as

$$0 \leqslant Pr_i = \frac{\lambda_i}{\sum \lambda} \leqslant 1 \Rightarrow H = -\sum_{i=1}^{3} Pr_i \log_3 Pr_i \quad 0 \leqslant H \leqslant 1 \tag{13}$$

When T_3 has only one non-zero eigenvalue, the entropy is zero for zero depolarization. When $H = 1$, T_3 is diagonal and maximum depolarization occurs. In practice this can be interpreted in the sense that for low entropy the backscatter is composed of only one scattering mechanism while for the high end we have a mixture of all different mechanisms. In the 30 cm resolution X-band SAR case the scattering entropy tends to be higher than at the relatively coarse L-band data. In order to select only reference points on flat ground terrain representing the base of each debris pile, a threshold of $H < 0.3$ is applied on the odd-bounce dominant areas. The basic idea of this approach is to find either man made surfaces like a "clean" part of an adjacent road or a base of a swept away house, etc., or to use land surfaces flattened by the flooding or even still inundated.

3.3. Debris height and volume estimation

An intuitive approach to estimate height information from remote sensing data is the use of stereoscopic radar images. The radargrammetric method (Leberl, 1990) was first proposed in the 1950s (Rinner, 1948), but due to the low spatial resolution in amplitude radar imaging on the one hand and to the development of high resolution InSAR based approaches on the other, it was rarely used until recent years. With the availability of new generations of high-resolution imagery acquired in spotlight modes from TerraSAR-X, COSMO-SkyMed, RADARSAT-2 and ALOS-2, the importance of radargrammetry is increasing. However, in the last decade only few groups have investigated radargrammetric applications for DEM generation from high-resolution spaceborne SAR data, e.g. Gutjahr et al. (2014) and Raggam et al. (2010) studied the potentials of the TerraSAR-X, (Toutin, 2010; Toutin and Chenier, 2009) the RADARSAT-2 and (Capaldo et al.,

Table 2
In situ measured pile heights and volumes as of August 25, 2013.

Id	w_1 [m]	w_2 [m]	l_1 [m]	l_2 [m]	h_1 [m]	h_2 [m]	h_3 [m]	Volume [m^3]	Shape code
1	10.49		22.37	–	4.28	–	–	1002.95	B
2	19.78	13.47	–	–	2.16	–	–	575.14	B
3	13.33	–	18.04	–	1.99	–	–	477.03	C
4	10.07	16.03	–	–	2.16	–	–	347.76	A
5	22.71	36.12	–	–	4.64	–	–	3802.02	B
6	23.38	19.6	43.9	–	2.46	6.69	–	747.37	G
7	23.31	22.93	13.06	11.75	4.46	–	–	1340.45	B + G
8	50.7	–	87.18	–	3.16	–	–	13945.18	F
9	87.01	79.55	46.6	44.82	5.77	3.12	8.16	23035.01	G + G
10	9.88	–	14.84	–	2.26	–	–	330.98	F
11	37.44	47.17	–	–	2.74	–	–	4838.96	A
12	32.52	26.08	48.81	–	4.29	–	–	6814.35	E
13	19.19	17.2	20.37	22.41	4.57	–	–	1785.42	B + G
14	17.78	16.62	11.54	13.15	3.72	–	–	764.18	G
15	40.16	–	81.22	–	3.41	–	–	11112.32	C
16	55.83	–	86.86	–	3.93	–	–	19073.55	F
17	26.31	32.49	43.14	–	2.61	1.36	–	2784.05	E
18	36.06	–	44.6	–	3.32	–	–	5344.93	F
19	174.57	166.22	36.91	32.17	2.84	5.96	6.02	31826.01	G + G
20	24.46	27.83	70.12	–	3.05	6.48	5.49	8585.97	D + D
21	17.8	13.54	40.66	–	5.36	–	–	3877.72	D

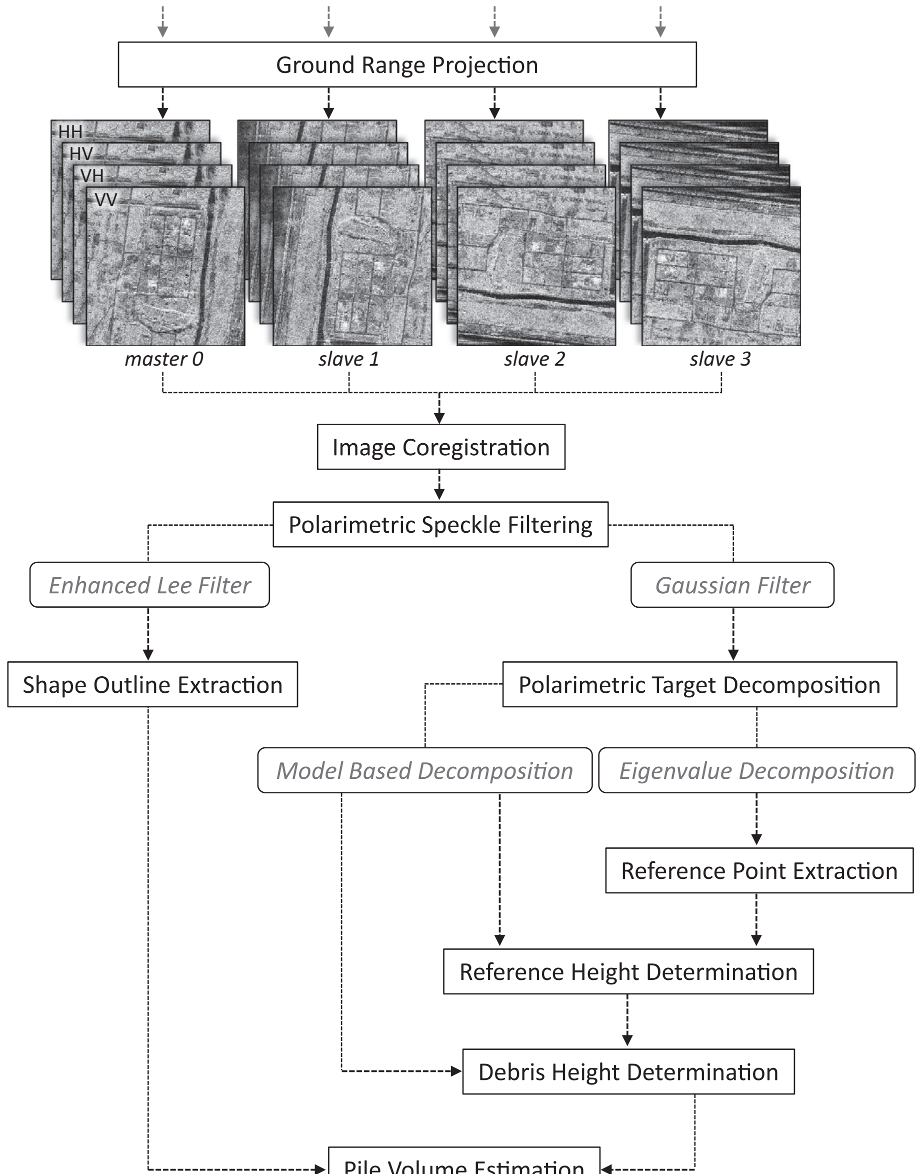

Fig. 9. Process flowchart of the proposed debris estimation method.

2011) the COSMO-SkyMed. Meric et al. (2011) used relatively coarse SIR-C data for DEM generation over the French Alps. Successful determination of building heights from airborne stereo SAR observations in urban environments based on the detection of salient lines and points in orthogonal-side images was demonstrated by Soergel et al. (2009). An approach for pixel-based building height estimation from spaceborne data by Dubois et al. (2013) relies only on the analysis of building layover in the disparity map. A PolSARgrammetric technique for building height estimation using coherency matrix components from fully polarimetric Pi-SAR data was developed by Dai et al. (2008) and Hamasaki et al. (2005). As compared to the standard relief modelling, these stereo SAR approaches for building height retrieval indeed have some relevance to the given study because the characteristic layover, foreshortening and overlapping effects in urban areas, at small scale, may approximate to debris piles.

Naturally, the optimum configuration to obtain good stereo geometry for radargrammetric applications is a set of two images observing the target from opposite sides. This however renders the image matching more intricate due to the large radiometric dissimilarities caused by the different imaging configurations as discussed in the forgoing section. Usually a same-side configuration is used where a pair with a base-to-height ratio ranging from 0.25 to 2 is seen as a good compromise (Meric et al., 2009). In the square-flight configuration used in this study, we have two stereo pairs orthogonal to each other. Fig. 11 shows a schematic of the two pairs of parallel flight paths, $S_1||S_2$ and $S_3||S_4$, imaging the target area in square-flight formation from altitudes h_i. After image coregistration, the target point P_t has the same x, y position and the along track separation is zero. The across-track separations are r_{d1} and r_{d2}, respectively. Both are computed from the accurate flight tracks of the Pi-SAR2 as recorded by DGPS with centimeter accuracy.

The scheme for the pixel-wise estimation of debris pile heights using a reference point P_r to define the pile base is shown in Fig. 12. The debris field is divided into rectangular cells of size Δx and Δy in the x and y direction, respectively. Considering the target pixel P_t located on the pile at the horizontal location $((n+1)\Delta x, y)$ with

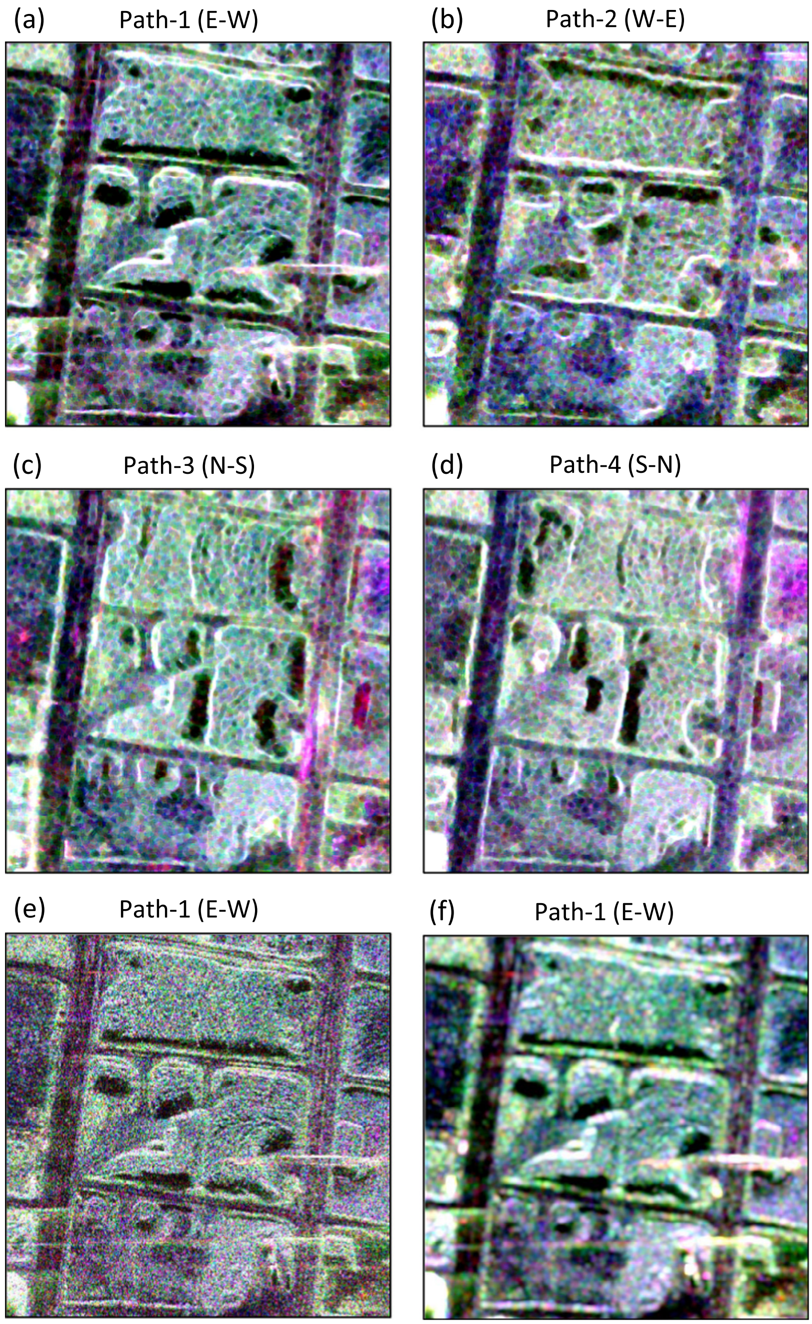

Fig. 10. Pauli RGB representations of Pi-SAR2 square-flight imaged debris field after coregistration with (a–d) Lee filtered, (e) unfiltered and (f) Gauss filtered results.

unknown height z_t and the reference object located at $(n\Delta x, y)$ with height $z_r = 0$, for stereo pair 1, the distances from P_t to S_1 and S_2 are R_1 and R_2, respectively. θ_1 is the angle between $\overline{P_tS_1}$ and $\overline{S_1S_2}$ given by the cosine law as

$$\theta_1 = \cos^{-1}\frac{R_1^2 + r_d^2 - R_2^2}{2R_1 r_d} \quad (14)$$

In practice, we have $\Delta x, z_t, z_r \ll R_{1r}, R_1$, and $\theta_1 > 30^\circ$. If $z_t > z_r$, the nominal case where the pile height is larger than the reference height, we observe that

$$R_1\Delta\theta_1 \cong \Delta x/\sin\theta_1 + (z_t - z_r - \Delta x\cot\theta_1)\cos\theta_1 \quad (15)$$

implying that $\Delta\theta_1 \cong 0$.

If $z_t \leqslant z_r$, we can observe that

$$R_{1r}\Delta\theta_1 \leqslant R_1\Delta\theta_1 \cong \Delta x/\sin\theta_1 \quad (16)$$

implying $\Delta\theta_1 \leqslant \Delta x/(R_{1r}\sin\theta_1) \cong 0$. It is important to note that, either way, we can approximate the $\Delta\theta_1$ term as zero.

The ranges $R_1 = |\overline{S_1P_t}|$ and $R_{1r} = |\overline{S_1P_r}|$ can be estimated from the SAR images data acquired from pass 1 and $\Delta R_1 = |\overline{AP_t}| = R_1 - R_{1r}$. The height difference Δz is then estimated as

$$\Delta z = z_r - z_t = |\overline{BC}| = \Delta R_1\cos\theta_1 \quad (17)$$

Consequently, if $z_r < z_t$, the pile height can be derived by

$$z_t = z_r - \Delta R_1\cos\theta_1 \quad (18)$$

where $\Delta R_1 < 0$.

Given the coordinates and height $z_r = 0$ of the reference ground point, the distances $R_{1r} = |\overline{S_1P_r}|$ and $R_{2r} = |\overline{S_2P_r}|$ can be calculated *a priori*. After computing the echo times from the target P_t and refer-

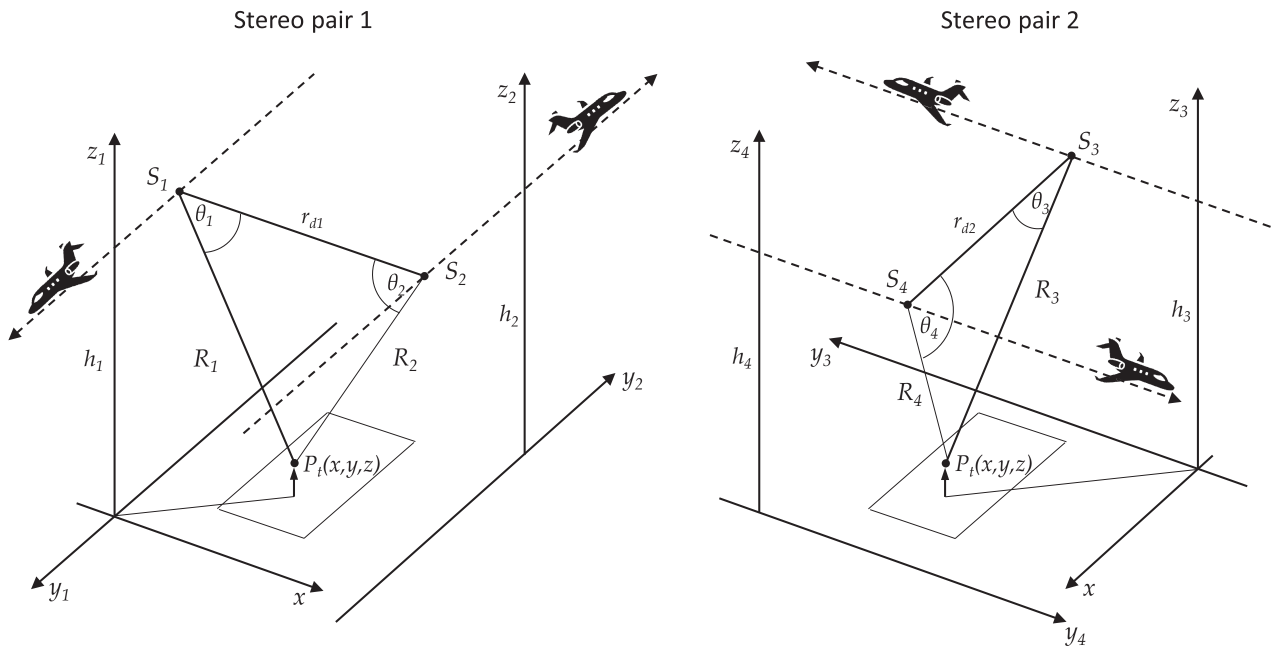

Fig. 11. Configuration of Pi-SAR2 square-flight paths over the target area.

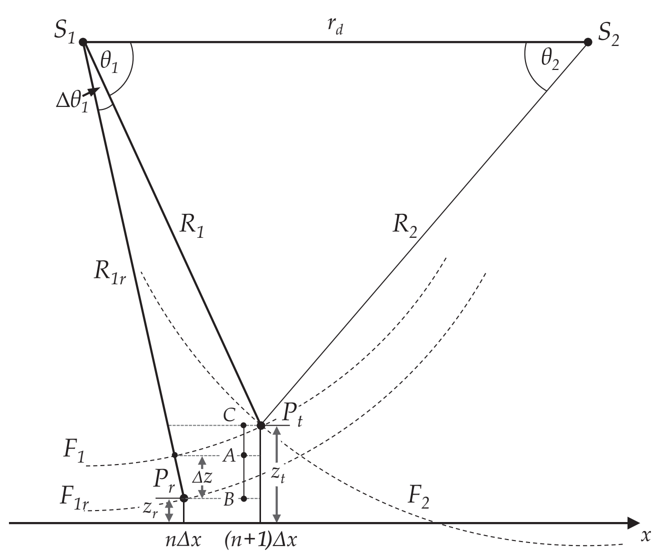

Fig. 12. Schematic of the estimation of θ_1 using R_1, R_2 and r_d and the subsequent height estimation using ΔR_1 and θ_1. F_1, F_{1r}, and F_2 represent the radar range fronts.

ence pixel P_r to S_1 as t_1 and t'_1, as well as to S_2 as t_2 and t'_2, respectively, the distances R_1 and R_2 are calculated as

$$R_1 = R_{1r} + \frac{c\Delta t_1}{2} \quad R_2 = R_{2r} + \frac{c\Delta t_2}{2} \tag{19}$$

where c is the speed of light, $\Delta t_1 = t_1 - t'_1$ and $\Delta t_2 = t_2 - t'_2$.

As the echo times are obtained directly from the Pi-SAR2 data, no phase synchronization between the two stereo pair images is required.

Subsequently, the height of the neighboring pixel located at $((n-1)\Delta x, y)$ is estimated in a similar fashion. Once the target height at $((n+1)\Delta x, y)$ and $((n-1)\Delta x, y)$ are obtained, they can be used as the reference height to estimate the heights at $((n+2)\Delta x, y)$ and $((n-2)\Delta x, y)$, respectively. By induction, this process is continued to derive the debris pile heights in the same row x at any given y position.

To obtain the base area of the debris piles we use a mathematical morphology analysis based approach (Haralick et al., 1987). After image fusion a Laplacian convolution filter with a 7×7 kernel size is applied to detect the shapes of each pile based on the strong reflection from the four foreshortened edges. Finally, the pile volumes are estimated on a voxel basis by summing up all the 3D cells (Δx, Δy, Δz) for each pile.

Possible errors in this approach might occur due to the non-visibility of the flat ground, because single debris pieces keep the entropy above the threshold. Consequently, no reference point can be found on the ground, and the height and volume determination may be biased. The same effect can occur in strongly vegetated surfaces which have not been flattened enough by the tsunami inundation. In some cases the algorithm might identify a reference area not at the base of a pile but at the top, if the shape is very flat. This is especially problematic for large man-made soil piles where the top may look exactly like the surrounding ground surface. For flooded conditions the reference height will be located at the water surface and not at the actual ground base of the piles. This may introduce an underestimation of the true target height. At the storage site in some cases the base of piles is some 20–40 cm lower than the road what can also lead to underestimation of the true height.

4. Results and discussion

The height information allows calculating the debris pile volume by using the area information obtained from the high resolution radar images. An example for a 3D reconstructed debris pile is shown in Fig. 13. The comparison between ground based and Pi-SAR2 derived pile heights for the stereopair $S_1||S_2$ is shown in Fig. 14. The retrievals are aligned well along the zero error line with a highly significant coefficient of determination of $R^2 = 0.87$. The root mean square error (RMSE) is 0.58 m. The comparison between volumes estimated from ground measured information and from Pi-SAR2 data is shown in Fig. 15. Note that due to the large span of the volume a logarithmic scale is used. The good accuracy of the retrieved pile heights allows estimating their volumes with an overall RMSE of 1099 m^3. We can observe that the voxel based volume estimates agree well with the in situ data over

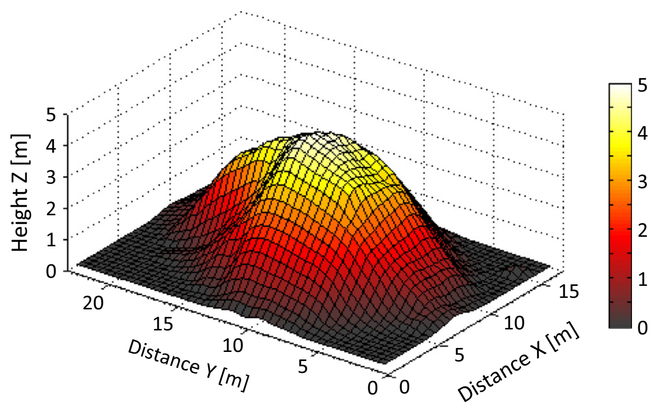

Fig. 13. Reconstructed debris pile.

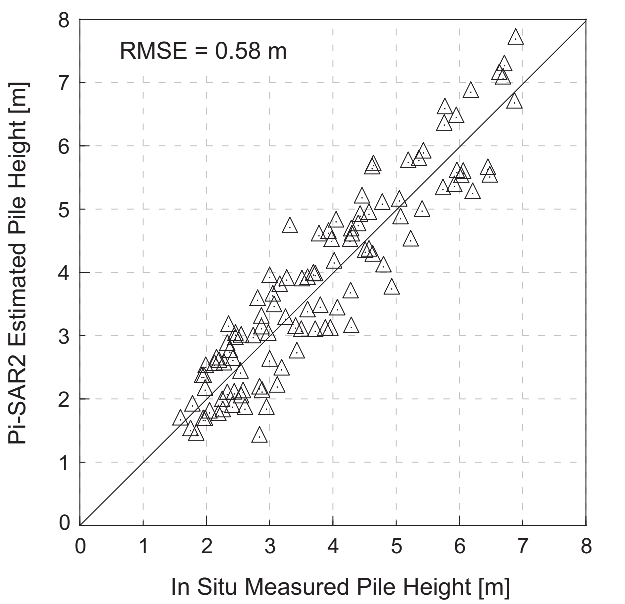

Fig. 14. Comparison between ground measured and Pi-SAR2 estimated heights of debris piles using the proposed method.

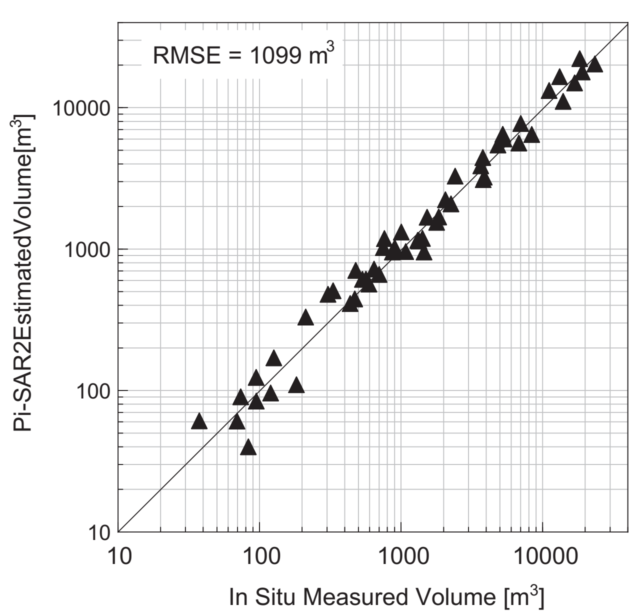

Fig. 15. Comparison between ground measured and Pi-SAR2 estimated debris volumes using the proposed method.

the whole volume range from the very small piles in the order of just 100 m^3 up to the very large piles with more than 20,000 m^3.

For comparison we also compute debris pile heights using the classical radargrammetric approach proposed by Leberl (1990). This approach relies on pixel-based normalized cross-correlation for image matching and employs a 3D space resection method together with range/Doppler equations for the height determination of image pixels. Without the use of a reference height point, while relying on the SRTM DEM, the RMSE is 1.24 m with a relatively low $R^2 = 0.51$ (Fig. 16). Note that, as the area is virtually flat, this error can only be attributed to a small extent to inaccuracies in the DEM but to the limitations of the classical technique.

The results for the debris pile volume estimation are shown in Fig. 17. The comparison against the volumes computed from the in situ data show poorer agreement than before. We can note that the majority of the pile volumes show a significant underestimation resulting in a RMSE of 2614 m^3. To proof that the larger error is not simply a result of the different ground heights used in the

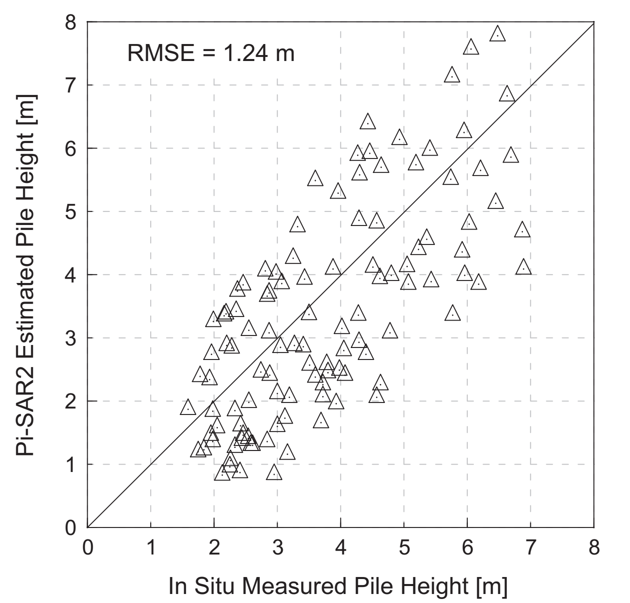

Fig. 16. Comparison between ground measured and Pi-SAR2 estimated heights of debris piles using the classical radargrammetric approach.

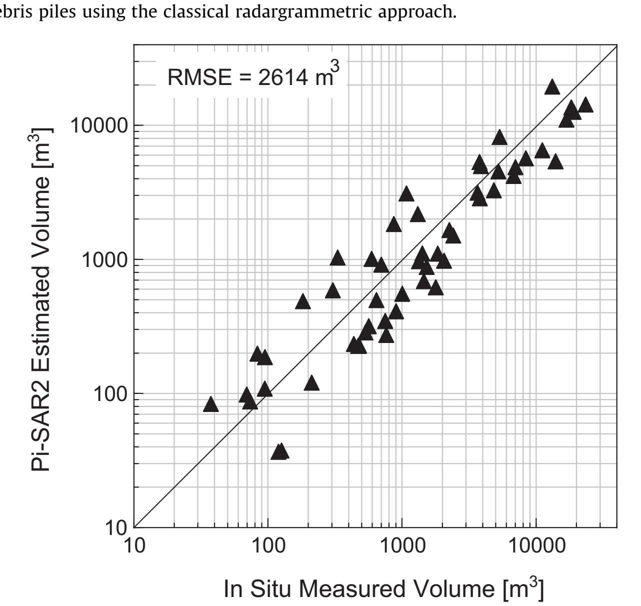

Fig. 17. Comparison between ground measured and Pi-SAR2 estimated debris volumes using the classical radargrammetric approach.

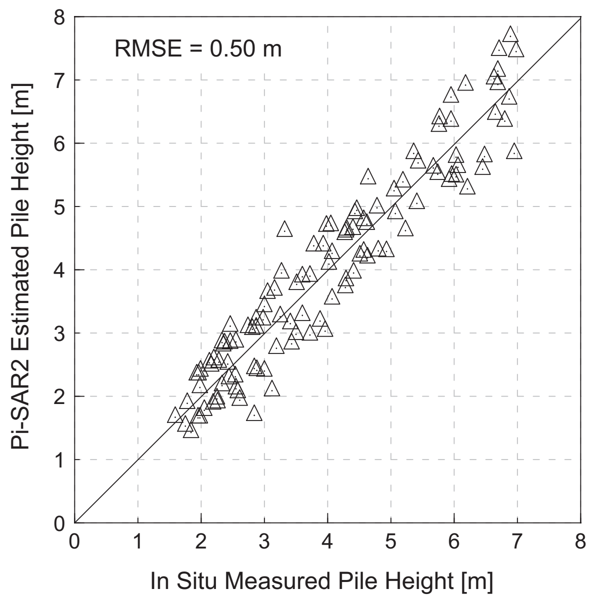

Fig. 18. Comparison between ground measured and Pi-SAR2 estimated heights of debris piles using the proposed method with two stereo-pairs.

proposed method and the standard method, we also calculated the pile heights using the standard method with the same reference heights as retrieved by the PolSAR approach described in Section 3.2. With the use of the individual base heights for each pile, the RMSE of the height estimates even slightly increases to 1.31 m ($R^2 = 0.50$). The accuracy of the volume estimation further decreases yielding a RMSE of 2874 m^3.

Finally, to investigate the virtue of having two orthogonal stereopairs available we combine the radargrammetric heights retrieved from both stereopairs $S_1||S_2$ and $S_3||S_4$. Using the average of both estimates, the RMSE can be reduced further to 0.50 m with a slightly better $R^2 = 0.90$ (Fig. 18). However, the improvements in the volume estimation are rather insignificant and thus it seems fair to say that a single stereopair is sufficient for the practical tsunami debris estimation.

For all the validation efforts, it is important to consider the errors that can occur due to the strategy for acquiring in situ data. In particular differences in the base area can introduce a large amount of uncertainty when computing the pile volumes. In fact, in this study, the horizontal pile geometry could be estimated more precisely from the SAR images as compared to the limited amount of ground based measurements by means of total station, laser ranger and GPS.

5. Conclusions

In order to help improving the emergency response after large scale disasters like earthquakes and tsunamis, we developed a novel approach for the estimation of heights and volumes of disaster debris piles. The proposed method based on radargrammetric surface height estimation using high resolution polarimetric stereo-SAR is relatively simple, robust and time efficient.

To achieve optimal image matching of the low-coherence noninterferometric data resulting from the illumination from opposite directions and in different polarizations, a gradient-based optical-flow estimation technique was used which has a number of advantages. Neither the relative phases nor auxiliary information such as topographic maps or DEM are required. The displacement is evaluated for each pixel and thus does not require the use of GCPs. The procedure significantly reduces the computational costs compared to conventional coregistration methods. Moreover, the suitability to combine multiresolution data offers opportunities to generate stereo SAR data by combining two different sensors. Most important, however, is the fact that the applied method allows precise coregistration of images taken under totally different viewing conditions.

To avoid unwanted multiple scattering contributions which could reduce the accuracy of echo time computation, we apply model based decomposition of the polarimetric scattering matrix and use only the odd-bounce components T_{odd} in the radargrammetric height estimation process. By considering only the relative height differences from the pile base to the top, and performing a voxel-based volume calculation, the estimation accuracy of both the heights and the resulting volumes of debris piles are well validated by comparison with in situ measurements.

To make the proposed method operational in a fully automated manner, future work has to be devoted to an automatic debris pile recognition. In this context, approaches based on feature extraction and simulation as recently reported by Kuny and Schulz (2014), who investigated debris of collapsed buildings in the city of Christchurch, seem promising. However, it should be noted that in our study no realistic, areally distributed post-event debris fields were taken into account while the investigation on automatic debris recognition should evidently be conducted on such datasets.

The use of two pairs of parallel flight paths from the square flight datasets showed slight improvements in the debris parameters estimation, however, in practical disaster mitigation application the use of only one pair seems to be quite sufficient. Hence, two parallel paths along the affected coastline would be sufficient while drastically decreasing the acquisition time and imaging area for improved response. Due to the aforementioned possibility to generate stereo SAR images by combining data from different sensors, a single-pass airborne image might be enough if a suitable satellite pass imaging the target from opposite, but parallel direction is available. Moreover, with increasing number of SAR satellites with right-and-left looking function, suitable stereo imaging could even be provided only from space.

We believe that the results presented in this paper give a promising outlook for drastically improved debris estimation by means of polarimetric radar imaging. With airborne or spaceborne systems ready for emergency response, results could be provided to decision makers within hours, regardless of time of day and weather conditions. Consequently, this study can hopefully contribute to improve disaster mitigation measures and disaster debris management in future events.

Acknowledgements

We gratefully acknowledge the financial support by JSPS Grant-in-Aid for Scientific Research (A) 23246076. We are most thankful to the National Institute for Communication and Information Technology (NICT) for the cooperation and provision of Pi-SAR2 image data through the PI program for collaborative research. Our special thanks go to Dr. Tatsuharu Kobayashi and Dr. Shoichiro Kojima of NICT as well as to the anonymous reviewers who helped improving this paper. We also thank the numerous Tohoku University students of Koshimura Lab and Sato Lab for the vital support in the ground measurements and the Sendai city authorities and subcontractors for their cooperation.

References

Aoki, Y., Arii, M., Koiwa, M., 2013. Spaceborne SAR data analysis for marine debris after the Great East Japan Earthquake. In: 2013 Asia-Pacific Conference on Synthetic Aperture Radar (APSAR), pp. 438–441.

Arii, M., Koiwa, M., Aoki, Y., 2014. Applicability of SAR to marine debris surveillance after the Great East Japan Earthquake. IEEE J. Select. Top. Appl. Earth Observ. Rem. Sens. 7, 1729–1744.

Asari, M., Sakai, S., Yoshioka, T., Tojo, Y., Tasaki, T., Takigami, H., Watanabe, K., 2013. Strategy for separation and treatment of disaster waste: a manual for earthquake and tsunami disaster waste management in Japan. J. Mater. Cycles Waste Manage. 15, 290–299.

Capaldo, P., Crespi, M., Fratarcangeli, F., Nascetti, A., Pieralice, F., 2011. High-resolution SAR radargrammetry: a first application with COSMO-SkyMed spotlight imagery. IEEE Geosci. Rem. Sens. 8, 1100–1104.

Chen, S.W., Sato, M., 2013. Tsunami damage investigation of built-up areas using multitemporal spaceborne full polarimetric SAR images. IEEE Trans. Geosci. Rem. Sens. 51, 1985–1997.

Chen, S.W., Wang, X.S., Xiao, S.P., Sato, M., 2014. General polarimetric model-based decomposition for coherency matrix. IEEE Trans. Geosci. Rem. Sens. 52, 1843–1855.

Chureesampant, K., Susaki, J., 2011. Automatic co-registration performance of fully polarimetric SAR images with texture relationship. In: 2011 IEEE International Geoscience and Remote Sensing Symposium (IGARSS), pp. 969–972.

Cloude, S.R., Pottier, E., 1996. A review of target decomposition theorems in radar polarimetry. IEEE Trans. Geosci. Rem. Sens. 34, 498–518.

Cloude, S.R., Pottier, E., 1997. An entropy based classification scheme for land applications of polarimetric SAR. IEEE Trans. Geosci. Rem. Sens. 35, 68–78.

Dai, E., Jin, Y.-Q., Hamasaki, T., Sato, M., 2008. Three-dimensional stereo reconstruction of buildings using polarimetric SAR images acquired in opposite directions. IEEE Geosci. Rem. Sens. 5, 236–240.

Dell'Acqua, F., Gamba, P., Lisini, G., 2004. Coregistration of multiangle fine spatial resolution SAR images. IEEE Geosci. Rem. Sens. 1, 237–241.

Dubois, C., Thiele, A., Hinz, S., 2013. Pixel-based approach for building heights determination by SAR radargrammetry. In: ISPRS Ann. Photogram. Remote Sens. Spatial Inf. Sci. II-3/W3, pp. 19–24.

Freeman, A., Durden, S.L., 1998. A three-component scattering model for polarimetric SAR data. IEEE Trans. Geosci. Rem. Sens. 36, 963–973.

Goto, K., Hashimoto, K., Sugawara, D., Yanagisawa, H., Abe, T., 2014. Spatial thickness variability of the 2011 Tohoku-oki tsunami deposits along the coastline of Sendai Bay. Mar. Geol. 358, 38–48.

Gutjahr, K., Perko, R., Raggam, H., Schardt, M., 2014. The epipolarity constraint in stereo-radargrammetric DEM generation. IEEE Trans. Geosci. Rem. Sens. 52, 5014–5022.

Hamasaki, T., Sato, M., Ferro-Famil, L., Pottier, E., 2005. Polarimetric SAR stereo using Pi-SAR square loop path. In: 2005 IEEE International Geoscience and Remote Sensing Symposium, 2005. IGARSS '05. Proceedings, p. 4.

Hansen, M., Howd, P., Sallenger, A., Write, W., Lillycrop, J.J., 2007. Estimation of post-Katrina debris volume: an example from coastal Mississippi. In: Farris, G. S., Smith, G.J., Crane, M.P., Demas, C.R., Robbins, L.L., Lavoie, D.L. (Eds.), Science and Storms—The USGS Response to the Hurricanes of 2005. U.S. Geological Survey, Reston, VA, pp. 43–48.

Haralick, R.M., Sternberg, S.R., Zhuang, X., 1987. Image analysis using mathematical morphology. In: IEEE Transactions on Pattern Analysis and Machine Intelligence PAMI-9, pp. 532–550.

Hardy, C.C., 1996. Guidelines for Estimating Volume, Biomass and Smoke Production for Piled Slash, Gen. Tech. Rep. PNW-GTR-364, Portland, OR.

Kobayashi, T., Umehara, T., Uemoto, J., Satake, M., Kojima, S., Matsuoka, T., Nadai, A., Uratsuka, S., 2012a. Damage detection of the great east Japan earthquake by the airborne SAR (PI-SAR2) of NICT. In: 2012 IEEE International Geoscience and Remote Sensing Symposium (IGARSS), pp. 4565–4566.

Kobayashi, T., Umehara, T., Uemoto, J., Satake, M., Kojima, S., Matsuoka, T., Nadai, A., Uratsuka, S., 2012b. Performance evaluation on cross-track interferometric SAR function of the airborne SAR system (PI-SAR2) OF NICT. In: 2012 IEEE International Geoscience and Remote Sensing Symposium (IGARSS), pp. 4529–4532.

Kobayashi, T., Umehara, T., Uemoto, J., Satake, M., Kojima, S., Matsuoka, T., Nadai, A., Uratsuka, S., 2014. Evaluation of digital elevation model generated by an airborne interferometric SAR (Pi-SAR2). In: 2014 IEEE International Geoscience and Remote Sensing Symposium (IGARSS), pp. 378–381.

Koyama, C.N., Hai, L., Sato, M., 2014. Pi-SAR2 square-flight imaging of tsunami affected area in Japan – surface parameter estimation by multi-aspect super high-resolution PolSAR data. In: Proceedings of EUSAR 2014; 10th European Conference on Synthetic Aperture Radar, pp. 1–4.

Koyama, C.N., Sato, M., 2014. Estimation of soil moisture and debris pile volume from Pi-SAR2X and Pi-SAR-L2 square-flight data. In: 2014 IEEE International Geoscience and Remote Sensing Symposium (IGARSS), pp. 1516–1519.

Krogager, E., Freeman, A., 1994. Three component break-downs of scattering matrices for radar target identification and classification. In: PIERS '94, Noordwijk, The Netherlands, p. 391.

Kuny, S., Schulz, K., 2014. Debris detection in SAR imagery using statistics of simulated texture. In: 2014 8th IAPR Workshop on Pattern Recognition in Remote Sensing (PRRS), pp. 1–4.

Le Besnerais, G., Champagnat, F., 2005. Dense optical flow by iterative local window registration. In: IEEE International Conference on Image Processing, 2005. ICIP 2005, pp. I-137–I-140.

Leberl, F.W., 1990. Radargrammetric Image Processing. Artech House, Norwood, MA.

Lee, J.-S., 1981. Speckle analysis and smoothing of synthetic aperture radar images. Comput. Graph. Image Process. 17, 24–32.

Lee, J.-S., Grunes, M.R., Ainsworth, T.L., Li-Jen, D., Schuler, D.L., Cloude, S.R., 1999. Unsupervised classification using polarimetric decomposition and the complex Wishart classifier. IEEE Trans. Geosci. Rem. Sens. 37, 2249–2258.

Lucas, B.D., Kanade, T., 1981. An iterative image registration technique with an application to stereo vision. Proceedings of the 7th International Joint Conference on Artificial Intelligence, vol. 2. Morgan Kaufmann Publishers Inc., Vancouver, BC, Canada, pp. 674–679.

Matsuoka, T., Umehara, T., Nadai, A., Kobayashi, T., Satake, M., Uratsuka, S., 2009. Calibration of the high performance airborne SAR system (Pi-SAR2). In: Geoscience and Remote Sensing Symposium, 2009 IEEE International, IGARSS 2009, pp. IV-582–IV-585.

Meric, S., Fayard, F., Pottier, E., 2009. Radargrammetric SAR image processing. In: Ho, P.-G.P. (Ed.), Geoscience and Remote Sensing. InTech, pp. 421–454.

Meric, S., Fayard, F., Pottier, E., 2011. A multiwindow approach for radargrammetric improvements. IEEE Trans. Geosci. Rem. Sens. 49, 3803–3810.

Plyer, A., Colin-Koeniguer, E., Weissgerber, F., 2015. A new coregistration algorithm for recent applications on urban SAR images. IEEE Geosci. Rem. Sens., 1–5

Plyer, A., Le Besnerais, G., Champagnat, F., 2014. Massively parallel Lucas Kanade optical flow for real-time video processing applications. J. Real-Time Image Proc., 1–18

Raggam, H., Gutjahr, K., Perko, R., Schardt, M., 2010. Assessment of the stereo-radargrammetric mapping potential of TerraSAR-X multibeam spotlight data. IEEE Trans. Geosci. Rem. Sens. 48, 971–977.

Ranghieri, F., Ishiwatari, M., 2014. Learning from Megadisasters: Lessons from the Great East Japan Earthquake. The World Bank.

Rinner, K., 1948. Die Geometrie des Funkbildes. Austrian Academy of Sciences, Math. Naturwiss. Klasse, also in Rinner, K., Benz F. 1966. In: Jordan, Eggert, Kneissl (Eds.), Handbuch der Vermessungskunde Band 6: Die Entfernungsmessung mit elektro-magnetischen Wellen und ihre geodatische Anwendung. Metzlersche Verlagsbuchandlung, Stuttgart.

Satake, M., Kobayashi, T., Uemoto, J., Umehara, T., Kojima, S., Matsuoka, T., Nadai, A., Uratsuka, S., 2012. Damage estimation of the Great East Japan earthquake with airborne SAR (PI-SAR2) data. In: 2012 IEEE International Geoscience and Remote Sensing Symposium (IGARSS), pp. 1190–1191.

Satake, M., Kobayashi, T., Uemoto, J., Umehara, T., Kojima, S., Matsuoka, T., Nadai, A., Uratsuka, S., 2013. Polarimetric calibration of Pi-SAR2. In: 2013 Asia-Pacific Conference on Synthetic Aperture Radar (APSAR), pp. 79–80.

Satake, M., Matsuoka, T., Umehara, T., Kobayashi, T., Nadai, A., Uemoto, J., Kojima, S., Uratsuka, S., 2011. Calibration experiments of advanced X-band airborne SAR system, Pi-SAR2. In: 2011 IEEE International Geoscience and Remote Sensing Symposium (IGARSS), pp. 933–936.

Sato, M., Chen, S.W., Satake, M., 2012. Polarimetric SAR analysis of tsunami damage following the March 11, 2011 East Japan Earthquake. P IEEE 100, 2861–2875.

Sato, R., Soma, K., Yajima, Y., Yamaguchi, Y., Yamada, H., 2007. Classification of stricken residential houses by the mid Niigata prefecture earthquake based on POLSAR image analysis. In: IEEE International Geoscience and Remote Sensing Symposium, 2007. IGARSS 2007, pp. 200–203.

Sendai City Environmental Bureau, 2012. Sendai City Waste Management Guidelines for Great East Japan Earthquake. Environmental Bureau, Sendai, Miyagi.

Soergel, U., Michaelsen, E., Thiele, A., Cadario, E., Thoennessen, U., 2009. Stereo analysis of high-resolution SAR images for building height estimation in cases of orthogonal aspect directions. ISPRS J. Photogr. Rem. Sens. 64, 490–500.

Suppasri, A., Koshimura, S., Imai, K., Mas, E., Gokon, H., Muhari, A., Imamura, F., 2012. Damage characteristics and field survey of the 2011 great East Japan tsunami in Miyagi Prefecture. Coast. Eng. J. 54. 125005-125001-125005-125030.

Tanikawa, H., Managi, S., Lwin, C.M., 2014. Estimates of lost material stock of buildings and roads due to the great East Japan earthquake and tsunami. J. Ind. Ecol. 18, 421–431.

Toutin, T., 2010. Impact of radarsat-2 SAR ultrafine-mode parameters on stereo-radargrammetric DEMs. IEEE Trans. Geosci. Rem. Sens. 48, 3816–3823.

Toutin, T., Chenier, R., 2009. 3-D radargrammetric modeling of RADARSAT-2 ultrafine mode: preliminary results of the geometric calibration. IEEE Geosci. Rem. Sens. 6, 282–286.

UNEP, 2012. Managing Post-disaster Debris: The Japan Experience. United Nations Environment Programme, Geneva, Switzerland, p. 51.

Watanabe, M., Motohka, T., Miyagi, Y., Yonezawa, C., Shimada, M., 2012. Analysis of urban areas affected by the 2011 off the Pacific coast of Tohoku earthquake and tsunami with L-band SAR full-polarimetric mode. IEEE Geosci. Rem. Sens. 9, 472–476.

Yamaguchi, Y., Singh, G., Kojima, S., Satake, M., Inami, M., Park, S., Cui, Y., Yamada, H., Sato, R., 2014. X-band 30 cm resolution fully polarimetric SAR images obtained by Pi-SAR2. In: 2014 IEEE International Geoscience and Remote Sensing Symposium (IGARSS), pp. 41–44.

Yamaguchi, Y., Yajima, Y., Yamada, H., 2006. A four-component decomposition of POLSAR images based on the coherency matrix. IEEE Geosci. Rem. Sens. 3, 292–296.

Yulianto, F., Sofan, P., Zubaidah, A., Sukowati, K.A.D., Pasaribu, J.M., Khomarudin, M. R., 2015. Detecting areas affected by flood using multi-temporal ALOS PALSAR remotely sensed data in Karawang, West Java, Indonesia. Nat. Hazards 77, 959–985.